

Article

Microstructure and Its Effect on the Intergranular Corrosion Properties of 2024-T3 Aluminum Alloy

Xiang Xiao ^{1,*}, Zeyu Zhou ¹, Cheng Liu ¹ and Lingfei Cao ^{2,*}

¹ Chinalco Materials Application Research Institute, Beijing 102209, China; zeyuhello@foxmail.com (Z.Z.); liucheng@cmari.com (C.L.)

² International Joint Laboratory for Light Alloys (Ministry of Education), College of Materials Science and Engineering, Chongqing University, Chongqing 400044, China

* Correspondence: xiang_xiao@chalco.com.cn (X.X.); caolingfei@cqu.edu.cn (L.C.); Tel.: +86-10-66600128 (X.X.); +86-23-65127306 (L.C.)

Abstract: Intergranular corrosion is the main corrosion type of Al-Cu-Mg aluminum alloys, which seriously reduce the lifetime of aircraft structural parts. In this paper, the microstructure and the intergranular corrosion behavior of 2024 alloy with varying Cu and Mg content were studied by using a scanning electron microscope (SEM), transmission electron microscope (TEM), and three-dimensional atom probe (3DAP). The results show that nano-scale θ (Al_2Cu) and S (Al_2CuMg) particles precipitate along grain boundaries after quenching. The nano-cluster is the main strengthening phase in the 2024 alloy after natural aging for 96 h. The intergranular corrosion susceptibility is greatly affected by the presence of θ (Al_2Cu) and S (Al_2CuMg) phases along grain boundaries. Specifically, Cu-rich precipitates and intermetallics are known to act as local cathodes, which facilitates the action of oxygen reduction and ultimately drives anodic dissolution of the surrounding matrix material. The intergranular corrosion resistance of the alloy decreases with the increase in Cu and Mg contents. The alloy with a lower Mg content shows better corrosion resistance than the commonly used one with a Cu to Mg mass ratio of 2.9. The relationship between the observed corrosion behavior and various contents of Cu and Mg elements is discussed, which has potential to benefit the composition design of 2xxx aluminum alloy with high corrosion resistance.

Keywords: 2024 aluminum alloy; Al-Cu-Mg; intergranular corrosion; composition; microstructure



Citation: Xiao, X.; Zhou, Z.; Liu, C.; Cao, L. Microstructure and Its Effect on the Intergranular Corrosion Properties of 2024-T3 Aluminum Alloy. *Crystals* **2022**, *12*, 395. <https://doi.org/10.3390/cryst12030395>

Academic Editors: Bolv Xiao and Evgeniy N. Mokhov

Received: 25 December 2021

Accepted: 7 March 2022

Published: 15 March 2022

Publisher's Note: MDPI stays neutral with regard to jurisdictional claims in published maps and institutional affiliations.



Copyright: © 2022 by the authors. Licensee MDPI, Basel, Switzerland. This article is an open access article distributed under the terms and conditions of the Creative Commons Attribution (CC BY) license (<https://creativecommons.org/licenses/by/4.0/>).

1. Introduction

The rapid development of aerospace industry has put forward higher requirements for the comprehensive properties of Al-Cu-Mg aluminum alloy (2xxx series alloys), which requires not only high strength and toughness, but also corrosion resistance [1,2]. Al-Cu-Mg aluminum alloys have wide applications in the aerospace industry due to their high specific strength, good fracture toughness, and excellent fatigue damage tolerance. The good mechanical properties partly result from alloying elements such as Cu. However, these 2xxx series alloys, alloying elements with Cu and Mg, are also susceptible to localized corrosion in chloride media such as pitting corrosion, intergranular corrosion (IGC), exfoliation, and stress corrosion cracking [3–5].

Intergranular corrosion is one of the most serious reasons for the material failure of Al-Cu-Mg aluminum alloys as aircraft structural parts. When intergranular corrosion occurs, the surface of the alloy may not change significantly, but the original physical and mechanical properties are almost completely lost. Since the intergranular corrosion is not easily observed, it often causes sudden damage to structural parts. Moreover, the detection of the incidence of intergranular corrosion is important from a maintenance perspective because it can develop into more severe forms of damage such as exfoliation, stress corrosion cracking (SCC), and fatigue cracking [6,7].

Many studies have been focused on the intergranular corrosion mechanisms in AA2024. S.P. Knight [8] used in situ synchrotron X-ray tomography to monitor the development of corrosion in 2024-T351 alloy and found that the initiation occurred at an intermetallic particle. R. Bonzom [9] described the IGC of 2024 aluminum alloy considering the dissolving paths with precipitated free zones at the grain boundaries where intermetallic precipitation occurred. W.L. Zhang [10] found that the growth kinetics for localized corrosion in AA2024-T3 exhibited a strong anisotropy, being slower in the short transverse or plate through-thickness direction than in either the longitudinal or long transverse directions. However, only a few quantitative measurements of the kinetics of IGC in Al alloys have been reported, and little is known about the influence of alloy content on localized corrosion behavior in 2024 aluminum alloy.

Therefore, in this paper, the microstructure and its effect on the intergranular corrosion behavior of 2024 alloy with varying Cu and Mg content was studied in detail. Attempts were made to explain the observed corrosion behavior of the alloy with various contents of Cu and Mg elements.

2. Materials and Methods

2.1. Materials

The materials used for the current study were 2024-T3 rolled plate from Chinalco Southwest Aluminum Co., Ltd. (Chongqing, China) with different contents of Cu and Mg elements. In order to study the effect of alloy element content on the intergranular corrosion performance of 2xxx alloy, alloys with different Cu and Mg contents were designed, with the ratio of Cu/Mg from 1.09 to 1.53, as shown in Table 1. Figure 1 shows the schematic diagram of the machining process of 2024 T3 plates. The T3 plate of 2 mm in thicknesses was treated in the following sequences: (1) homogenization, (2) hot rolling, (3) cold rolling, (4) solution treatment with different quenching transfer time for 14, 30, and 50 s, and (4) natural ageing at room temperature for 96 h. Figure 1 shows the schematic diagram of deformation and heat treatment processes used for 2024 T3 plates.

Table 1. The compositions of 2024 T3 plates with different contents of Cu and Mg.

Materials	Wt%						Cu/Mg
	Si	Fe	Cu	Mn	Mg	Zn	
1#	0.040	0.23	4.78	0.67	1.17	0.012	1.53
2#	0.034	0.22	4.07	0.67	1.04	0.011	1.47
3#	0.041	0.23	4.96	0.45	1.39	0.012	1.34
4#	0.034	0.21	4.46	0.44	1.19	0.011	1.41
5#	0.044	0.22	4.8	0.62	1.57	0.014	1.15
6#	0.035	0.18	4.14	0.62	1.42	0.011	1.09
7#	0.043	0.23	5.53	0.48	1.82	0.013	1.14
8#	0.035	0.19	4.56	0.47	1.55	0.011	1.10

stands for sample number.

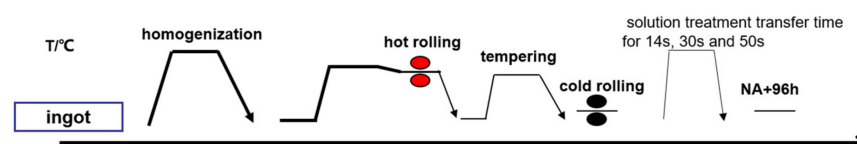


Figure 1. Schematic diagram of deformation and heat treatments used for 2024-T3 plates.

2.2. Tests Methods

Tests consisting of immersion in a corrosive solution followed by optical observations on sectioned samples were carried out. All testing was performed on the plane with its normal along the short transverse direction. The morphology of the residual phase and precipitates were analyzed using a JSM 7800F (Japan) scanning electron microscopy (SEM),

JSM 7800F (Japan) energy dispersive X-ray spectrometry (EDS), and FEI Tecnai G2 F20 (USA) transmission electron microscopy (TEM) techniques. The second phase was tested and analyzed using a JSM 7800F scanning electron microscope with Oxford X-max50 EDS. Before the test, the samples were mechanically polished with 2000-grit SiC paper, and the surface was cleaned with alcohol solution.

The intergranular corrosion tests samples with a size of $40 (L) \times 25 (T) \times 2 (S) \text{ mm}^3$ were machined from the 2024-T3 plate and degreased in ethanol. All samples were mechanically polished with up to 4000 grits SiC paper in water, followed by cleaning in ethanol and air drying. After that, the samples were corroded with 10% NaOH solution for 5–10 min, and then cleaned in 30% HNO₃ solution. All samples were then exposed to the solutions (NaCl 30 g, HCl 10 mL, deionized water 1 L) at the temperature of $35 \pm 1 \text{ }^\circ\text{C}$ for 24 h according to the Standard HB 5255. After immersion, the samples were cleaned in 30% nitric acid, air dried, and stored in a desiccator.

A square sample with a size of $1 \times 1 \text{ cm}^2$ was cut, and the surface to be tested was polished and then subjected to the potential-current (PD) curve test. An Electrochemical Impedance Spectroscopy (EIS) test and Tafel cyclic polarization curve test were performed in 3.5% NaCl solution for 30 min. All testing was kept at a constant temperature. A Tafel cycle polarization curve was used to obtain self-corrosion potential, self-corrosion current, and other parameters.

The transmission electron microscopy (TEM) observation and selected area electron diffraction (SAED) pattern measurements were carried out on an FEI Tecnai G² F20 microscope. Samples with a diameter of 3 mm were mechanically polished and twin jet electropolished in a solution mixed with 1 volume of HNO₃ and 3 volumes of methanol at $-30 \text{ }^\circ\text{C}$.

A three-dimensional atom probe (3DAP) was used to study the distribution of alloying elements. The needle-like tips were prepared by standard two-stage electropolishing, and data probing was performed on a Cameca LEAP 4000HR in an ultrahigh vacuum condition. The specimen temperature was about $-248 \text{ }^\circ\text{C}$, pulse fraction was 15% with a detector efficiency of 36%. The data analysis was performed by using the IVAS 3.8 software (China). The clusters were analyzed by setting the different maximum separation distance (d_{max}) as 0.7 nm with a minimum atom number of 10.

3. Results and Discussion

3.1. Microstructure Observation

It is well known that the susceptibility to intergranular corrosion and to other localized corrosion is caused by the microstructure of the alloy. The high strength of the 2024-T3 plate presents recrystallization grains with the size ranging from 20 to 50 μm . SEM observations performed on the 2024 alloy show the presence of a uniform distribution of coarse intermetallic particles, as presented in Figure 2. The size of these coarse particles increases to 10 μm . The EDS analysis on these second phase particles shown in Figure 2 indicates that there are two types of precipitates, namely Al-Cu-Mg particles, which can be assigned as Al₂CuMg (S phase), and irregularly shaped Al-Cu-Mn-Fe containing particles.

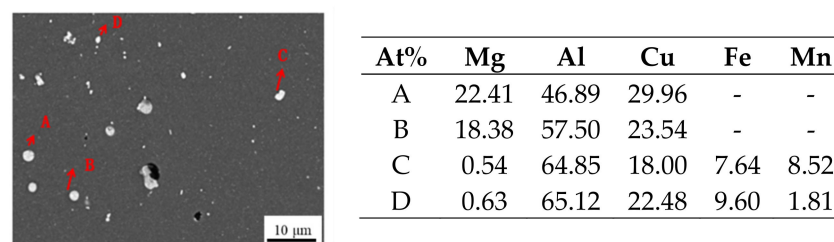


Figure 2. Coarse intermetallic particles in 2024 alloy and corresponding EDS results.

To investigate the smaller particles (micron and nanometer scale) in the matrix and along the grain boundary, the observations by TEM were further performed, as shown in Figure 3. EDS and the diffraction pattern analysis were also used to determine the particle

type, seen in Figures 4–6. It is worth noting that no precipitate free zone can be observed along the grain boundary as shown in Figure 3. The rod shaped Al-Cu-Mn dispersoids are homogeneously distributed in the matrix with an average length of 200 nm which can be seen in Figure 3e,f.

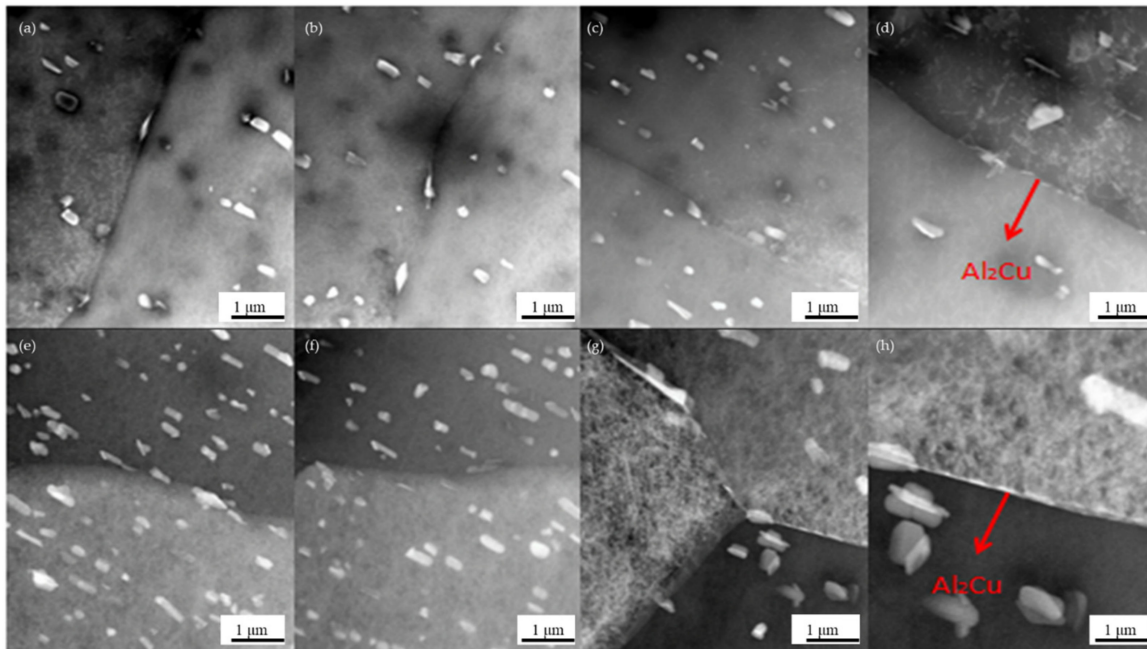


Figure 3. (a–h) The TEM images of 2024 alloy in the matrix and along the grain boundary.

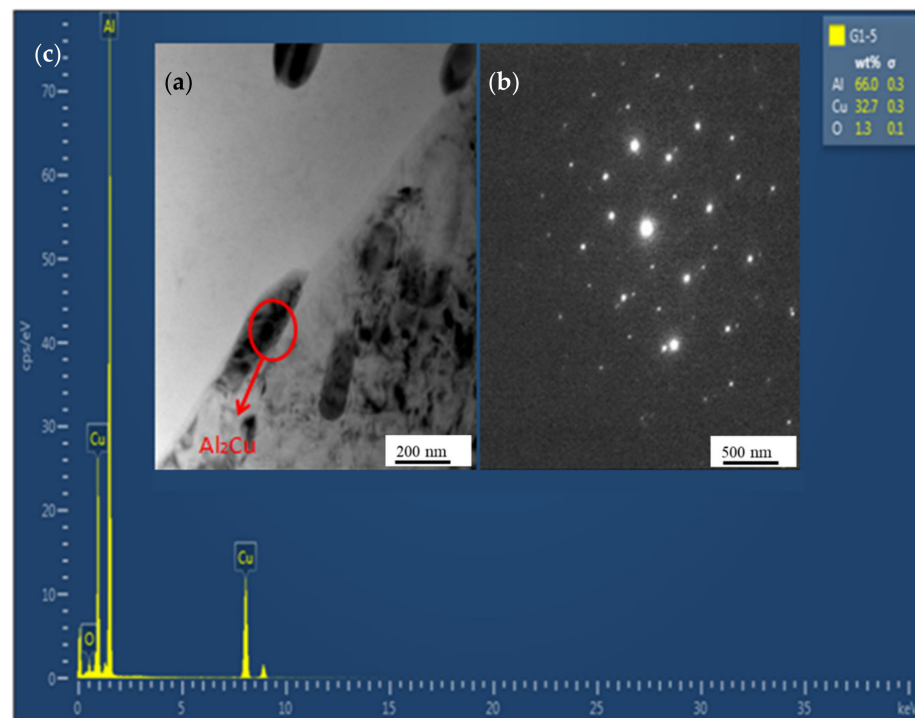


Figure 4. The morphology of Al_2Cu particle precipitated along the grain boundary (a), and the corresponding diffraction pattern (b) and EDS result (c).

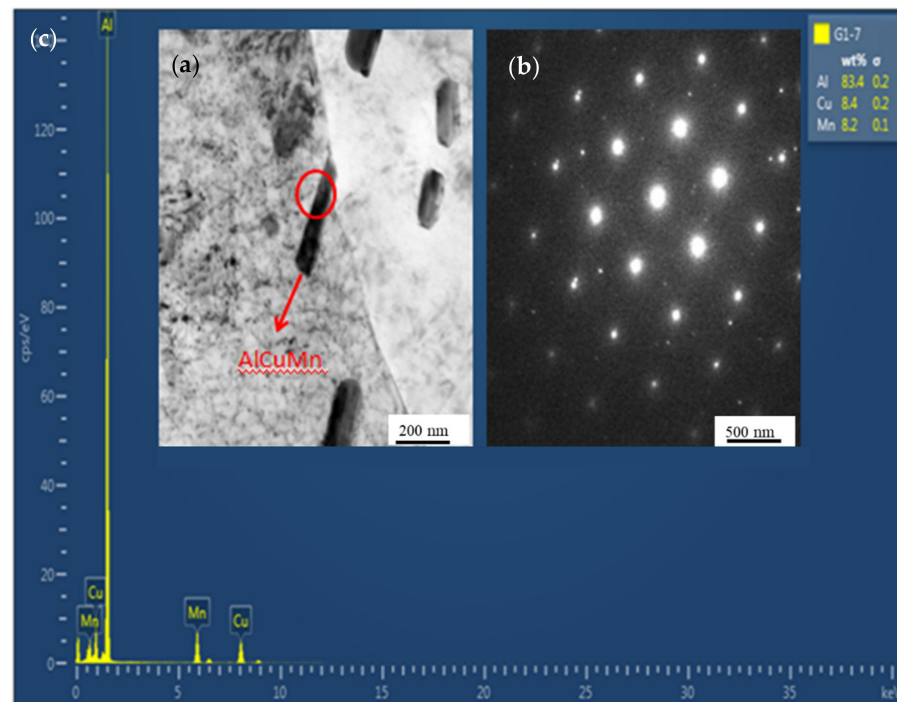


Figure 5. The morphology of AlCuMn particle precipitated along the grain boundary (a), and the corresponding diffraction pattern (b) and EDS result (c).

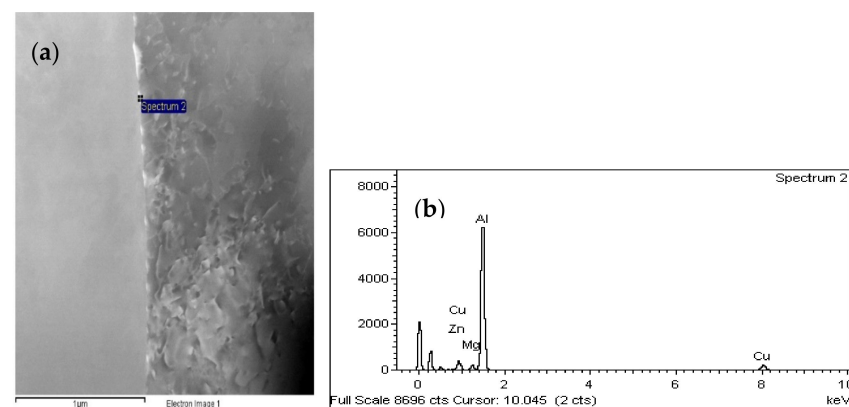


Figure 6. The morphology of AlCuMg particle precipitated along the grain boundary (a) and the EDS results (b).

Needle shaped particles with nano-scale precipitate along the interface of grain can be found in Figure 3d,g,h. To further determine the types of these particles, we used the combined method of the EDS and diffraction pattern. The results from Figures 4–6 show that the second phases precipitated in the grain boundary included (1) the nano-scale Al_2Cu phase with an average length of 100 nm (Figure 4); (2) the rod-shaped Al-Cu-Mn dispersoids with an average length of 200 nm (Figure 5); (3) the nano-scale Al_2CuMg phase with an average length of 20 nm (Figure 6); (4) the Al-Cu-Mn-Fe containing phase. It is worth noting that the Al-Cu-Mn dispersoids are precipitated during the homogenization process, and the Al-Cu-Mn-Fe containing phase is formed during solidification, while the nano-scale Al_2Cu phase and Al_2CuMg phase are precipitated during quenching. In addition, the precipitates along the grain boundary are heterogeneous as well. Only a few grain boundaries can be found the presence of nano-scale particles. Even more, the nano-scale Al_2Cu phase and Al_2CuMg phase cannot be found in the matrix as well.

The 3DAP results in Figure 7 show that after natural ageing for 96h, the atom segregation formed in the matrix. The nano-sized clusters can be detected, which are the main strengthening phase in the 2024-T3 alloy. The average equivalent radius of cluster can be calculated as 0.64 nm and the density of the cluster is about $6.92 \times 10^{24}/\text{nm}^3$. The composition of the cluster is around 42.74 at% Al, 28.35 at% Cu, 28.66 at% Mg, 0.06 at% Mn, 0.05 at% Zn, which is close to the assigned chemical composition of Al_2CuMg (S phase). It seems that in the 2024-T3 plate, the precipitation strengthening (cluster effect) may be a main strengthening method.

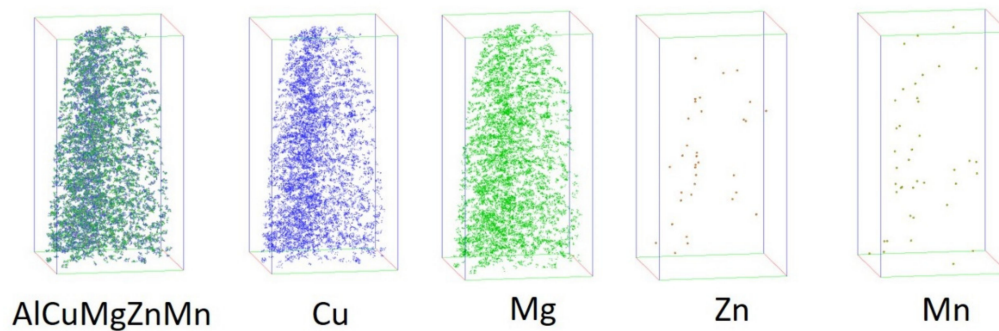


Figure 7. The cluster maps of the 2024-T3 plate by 3DAP.

It can be summarized that the second phases precipitated in the grain include coarse Al-Cu-Mn-Fe and S phase (formed during solidification), Al-Cu-Mn dispersoids (formed during homogenization), and cluster- Al_2CuMg (formed during NA). The second phases precipitated along the grain boundary include Al_2CuMg and Al_2Cu phase (formed during quenching), Al-Cu-Mn-Fe (formed during solidification), and Al-Cu-Mn dispersoids (formed during homogenization).

3.2. Intergranular Corrosion

Figure 8 depicts the optical images of 2024-T3 plate on sectioned samples after corrosion. There are deep corrosion holes in the alloy surface area, and there is no corrosion or slight corrosion in other areas, as shown in Figure 8(a1,b1,c1,d1). The corrosion type of 2024-T3 plate with a short quenching transfer time can be determined as pitting corrosion. It is obvious that with the quenching transfer time prolonged, the corrosion depth for each alloy is increased. It extends along the interface between different grains. As seen from Figure 9(d3), there is a network corrosion morphology along the grain boundary. The corrosion type of 2024-T3 plate with a longer quenching transfer time is intergranular corrosion. This is mainly due to the precipitation of nano particles on the grain boundary with the extension of quenching transfer time, which intensifies the sensitivity of intergranular corrosion. It has been reported that IGC starts with the dissolution of the S phase on grain boundaries caused by the galvanic coupled solute-depleted zone/surrounding matrix and solute-depleted zone/S phase particles. Then, IGC propagates due to the dissolution of the copper depleted zone along the grain boundaries. The statistical results of the maximum corrosion depth and average of corrosion depth for the three different quenching transfer times (14, 30, and 50 s) of the different alloys are shown in Table 2. It can be seen that the corrosion image and the depth are different for the alloys with different contents of Cu and Mg elements.

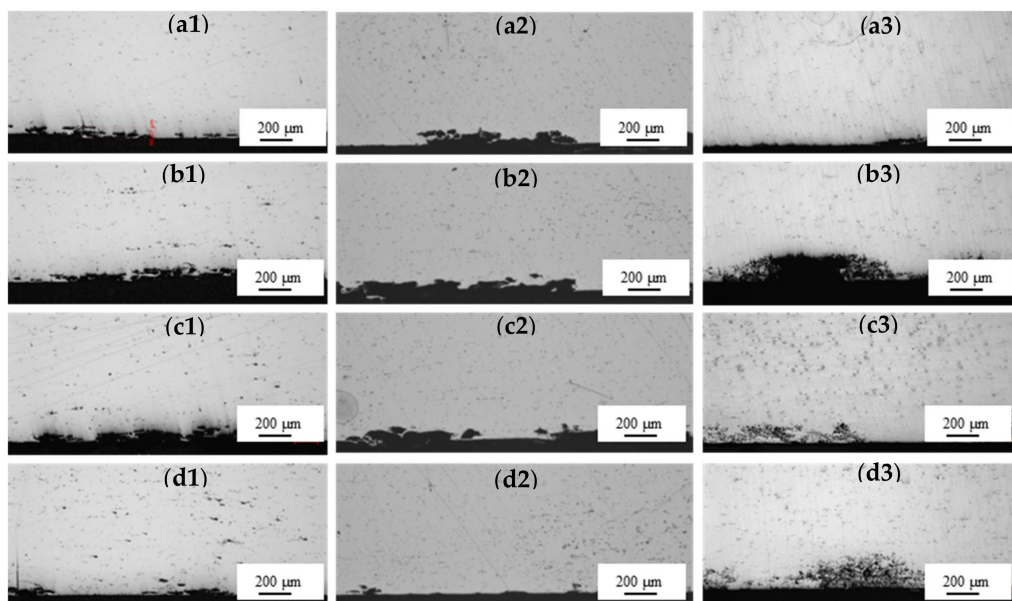


Figure 8. Metallographic cross sections showing localized corrosion morphologies with different alloy at different quenching transfer times (a) 2#-Cu/Mg = 1.47 ((a1)—14 s; (a2)—30 s; (a3)—50 s), (b) 4#-Cu/Mg = 1.41 ((b1)—14 s; (b2)—30 s; (b3)—50 s), (c) 6#-Cu/Mg = 1.09 ((c1)—14 s; (c2)—30 s; (c3)—50 s), (d) 8#-Cu/Mg = 1.1 ((d1)—14 s; (d2)—30 s; (d3)—50 s).

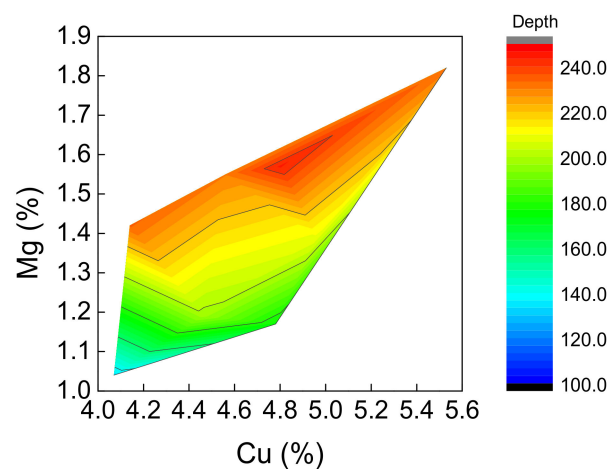


Figure 9. The effect of Cu and Mg on the average corrosion depth of 2024 alloy.

Table 2. The maximum and average of corrosion depth for the different alloy samples with different quenching transfer time.

Materials	The Maximum Depth/ μm			Average Depth/ μm
	14 s	30 s	50 s	
1#	126	183	218	176
2#	126	132	146	135
3#	140	181	306	209
4#	154	170	270	198
5#	180	178	374	244
6#	199	187	316	234
7#	156	195	343	231
8#	138	225	328	230

The effect of Cu and Mg on the average corrosion depth of 2024 alloy can be described in Figure 9. It seems that for the developed 2024 alloy, increasing the content of Cu and Mg makes the intergranular corrosion performance become worse. It is also worth noting that the effect of Mg content on the corrosion depth is greater than that of Cu.

3.3. Electrochemical Behavior

The Nyquist plots of the alloy with various Cu/Mg tested in the 3.5 wt.% NaCl solution are shown in Figure 10. The equivalent circuit diagram selected according to Nyquist plot is shown in Figure 11. The typical polarization curves of the alloys in another 3.5 wt.% NaCl solution are shown in Figure 12. The values of layer capacitance Cd, passivation film resistance Rp, and corrosion current can be then obtained by using equivalent circuit processing, as shown in Table 3. It is clear that with the increase in Cu/Mg ratio, the value of Rp increases and the corrosion current decreases, which means that the corrosion resistance of the alloy is improved.

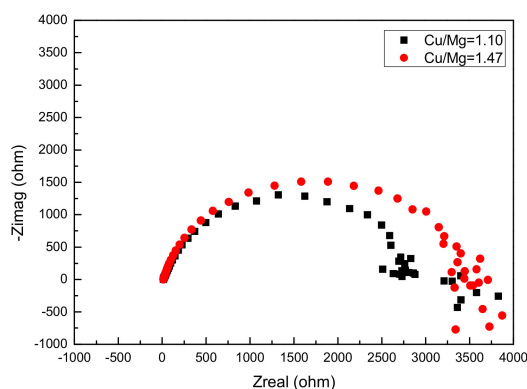


Figure 10. Nyquist plot of the alloy.

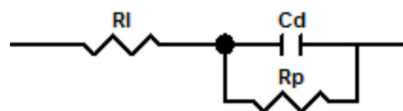


Figure 11. The equivalent fitting circuit.

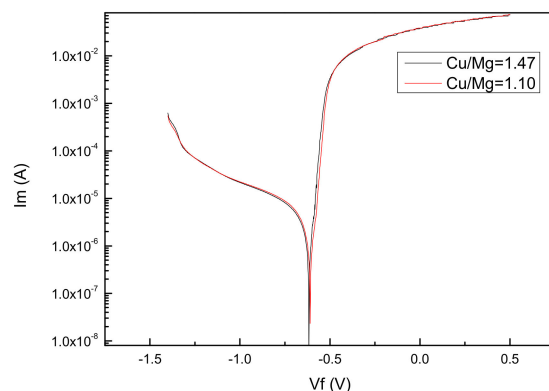


Figure 12. Polarization curves of the alloy.

Table 3. Corrosion parameters of the alloy.

Cu/Mg	Cd/(S·sp·cm ⁻²)	Rp/(Ω·cm ²)	Corrosion Current (μA)
1.10	6.49 × 10 ⁻⁶	2554	3.13
1.47	9.15 × 10 ⁻⁶	3180	2.87

There is a large section of capacitive reactance arc in Nyquist plot, so the time constant can be regarded as one. Additionally, the equivalent fitting circuit (Figure 11) was used to obtain the solution resistance R_1 , layer capacitance C_d , and passivation film resistance R_p .

Previous studies [8–12] have shown that the potential difference between grain boundaries and adjacent grains is the driving force of intergranular corrosion, and the characteristics of grain boundaries and adjacent regions, including chemical composition, morphology, and distribution of precipitates, play a key role in the sensitivity of intergranular corrosion. Figure 13 shows the isothermal section of Al-Cu-Mg alloy at 200 °C calculated by Pandat 2013 software (add in China). It seems that in the composition range of 2024 alloy, the equilibrium phase at 200 °C is located in the (Al₂Cu + Al₂CuMg + FCC) three-phase region. Increasing the content of Mg element can promote the precipitation of Al₂CuMg (S-phase). According to the experimental results, the microstructure of 2024-T3 plate consists of coarse Al₂CuMg (S-phase) constituents. Moreover, the nano-scale Al₂CuMg particles can be formed along the grain boundary during quenching. It was reported that the corrosion rate of Al₂CuMg phase is much higher than pure aluminum. This is mainly due to the fact that the Mg element in S phase is easy to dissolve, and the deposited Cu element after corrosion can increase the electrode potential of the particles, thus accelerate the dissolution of Mg [13].

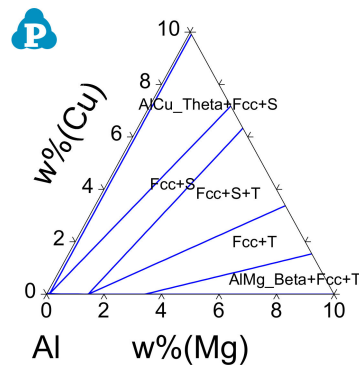


Figure 13. The isothermal section of Al-Cu-Mg alloy at 200 °C calculated by Pandat software.

Figure 14 shows the electrode potential of fcc matrix of Al-4Cu alloy, copper-poor area, and the particles. It can be seen that the electrode potential of S phase is lowest among the fcc, copper-poor area, and other particles. In the initial stage of corrosion, S phase is dissolved preferentially. With the corrosion proceeding, the enrichment of inactive element Cu in S phase results in the positive potential of S phase and the negative potential of the copper-poor area. Thus, a corrosion micro-couple with the copper-poor area can be established, leading to anodic dissolution in the copper-poor area. In addition, the copper-poor region is always an anode relative to the matrix, and the galvanic corrosion between them can accelerate the intergranular corrosion. It is also found that the potential of Al₂Cu phase is higher than that of the copper-poor area and matrix. During the corrosion process, pitting corrosion occurs in the copper-poor area around the Al₂Cu phase. With the corrosion proceeding, the pitting holes are connected to each other and form corrosive channels along the grain boundary [14–16]. S phase is dissolved firstly to form pits as positive electrode. With the corrosion proceeding, the enrichment of inactive element Cu in S phase can cause the positive potential of S phase and the negative potential of the copper-poor area.

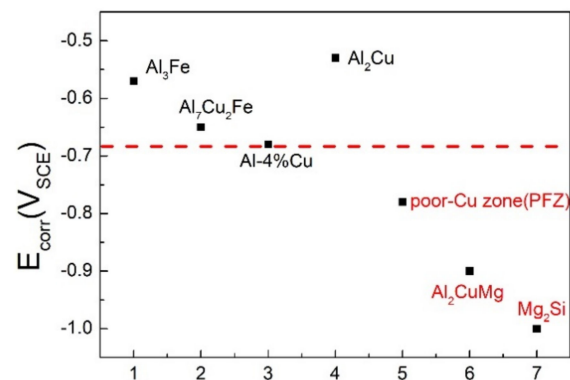


Figure 14. The electrode potential of fcc Al, copper-poor zone, and particles.

Figure 15 shows the schematic illustration of corrosion mechanism in 2xxx series alloys. It can be explained by a galvanic coupling between copper rich particles (θ - Al_2Cu ; S- Al_2CuMg) and the grain boundary. Therefore, for the composition design of 2xxx alloy with good corrosion resistance, the Mg content should be reduced to the lowest priority, while the Cu content should be reduced appropriately [17,18].

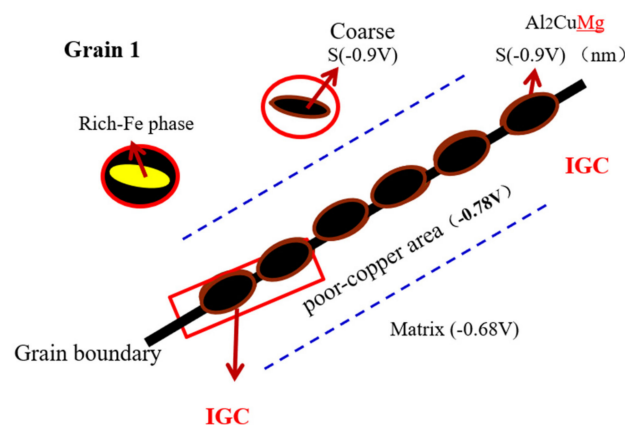


Figure 15. Corrosion mechanism of 2xxx series aluminum alloys.

4. Conclusions

In this paper, the microstructure and its effect on the intergranular corrosion behavior of 2024 T3 alloy was studied in detail using a scanning electron microscope (SEM), transmission electron microscope (TEM), and three-dimensional atom probe (3DAP). The results can be summarized below:

- (1) There are nano-scale θ (Al_2Cu) and S (Al_2CuMg) particles along grain boundaries after quenching. The nano-cluster is the main strengthening phase in the 2024 alloy after natural aging for 96 h. The intergranular corrosion susceptibility is greatly affected by the presence of θ (Al_2Cu) and S (Al_2CuMg) phases along the grain boundary. Specifically, Cu-rich precipitates and intermetallics are known to act as local cathodes, which facilitate oxygen reduction reactions and ultimately drive anodic dissolution of the surrounding matrix.
- (2) The intergranular corrosion resistance of the alloy decreases with the increasing content of Cu and Mg elements. The results also show that the corrosion resistance of 2024 alloy with lower Mg content is significantly improved as compared with the 2024 alloy with a more common composition (Cu to Mg mass ratio of 2.9).

Author Contributions: Data curation, Z.Z.; Formal analysis, L.C.; Methodology, C.L.; Writing—original draft, X.X. All authors have read and agreed to the published version of the manuscript.

Funding: This research received no external funding.

Data Availability Statement: Relevant research data can be found at Chinalco Materials Research Institute Co., Ltd. or Chongqing University.

Conflicts of Interest: The authors declare no conflict of interest.

References

1. Staszczuk, A.; Sawicki, J.; Adamczyk-Cieslak, B. A study of second-phase precipitates and dispersoid particles in 2024 aluminum alloy after different aging treatments. *Materials* **2019**, *12*, 4168. [[CrossRef](#)] [[PubMed](#)]
2. Lin, Y.C.; Xia, Y.C.; Jiang, Y.Q.; Zhou, H.M.; Li, L.T. Precipitation hardening of 2024-T3 aluminum alloy during creep aging. *Mater. Sci. Eng. A* **2013**, *565*, 420–429. [[CrossRef](#)]
3. Merati, A. A study of nucleation and fatigue behavior of an aerospace aluminum alloy 2024-T3. *Int. J. Fatigue* **2005**, *27*, 33–44. [[CrossRef](#)]
4. Huda, Z.; Taib, N.I.; Zaharinie, T. Characterization of 2024-T3: An aerospace aluminum alloy. *Mater. Chem. Phys.* **2009**, *113*, 515–517. [[CrossRef](#)]
5. Yu, X.X.; Sun, J.; Li, Z.T.; Dai, H.; Fang, H.J.; Zhao, J.F.; Yin, D.F. Solidification behavior and elimination of undissolved Al₂CuMg phase during homogenization in Ce-modified Al–Zn–Mg–Cu alloy. *Rare Met.* **2020**, *39*, 1279–1287.
6. Sebastian, D.; Yao, C.W.; Lian, I. Multiscale corrosion analysis of superhydrophobic coating on 2024 aluminum alloy in a 3.5 wt% NaCl solution. *MRS Commun.* **2020**, *10*, 305–311. [[CrossRef](#)]
7. Blanc, C.; Gastaud, S.; Mankowski, G. Mechanistic studies of the corrosion of 2024 aluminum alloy in nitrate solutions. *J. Electrochem. Soc.* **2003**, *150*, B396. [[CrossRef](#)]
8. Knight, S.P.; Salagaras, M.; Wythe, A.M.; de Carlo, F.; Davenport, A.J.; Trueman, A.R. In situ X-ray tomography of intergranular corrosion of 2024 and 7050 aluminium alloys. *Corros. Sci.* **2010**, *52*, 3855–3860. [[CrossRef](#)]
9. Bonzom, R.; Oltra, R. Intergranular corrosion propagation rate of 2024 alloy investigated via the “one-dimensional artificial pit” technique. *Corros. Sci.* **2016**, *111*, 850–855. [[CrossRef](#)]
10. Zhang, W.L.; Frankel, G.S. Localized Corrosion Growth Kinetics in AA2024 Alloys. *J. Electrochem. Soc.* **2002**, *149*, 510–519. [[CrossRef](#)]
11. Zhang, X.X.; Zhou, X.R.; Hashimoto, T.; Liu, B. Localized corrosion in AA2024-T351 aluminium alloy: Transition from intergranular corrosion to crystallographic pitting. *Mater. Charact.* **2017**, *130*, 230–236. [[CrossRef](#)]
12. DeRose, J.A.; Suter, T.; Bałkowiec, A.; Michalski, J.; Kurzydowski, K.J.; Schmutz, P. Localised corrosion initiation and microstructural characterisation of an Al 2024 alloy with a higher Cu to Mg ratio. *Corros. Sci.* **2012**, *55*, 313–325. [[CrossRef](#)]
13. Alexopoulos, N.D.; Papanikos, P. Experimental and theoretical studies of corrosion-induced mechanical properties degradation of aircraft 2024 aluminum alloy. *Mater. Sci. Eng. A* **2008**, *498*, 248–257. [[CrossRef](#)]
14. Ghosh, K.S.; Hilal, M.; Sagnik, B. Corrosion behavior of 2024 Al–Cu–Mg alloy of various tempers. *Trans. Nonferrous Met. Soc. China* **2013**, *23*, 3215–3227. [[CrossRef](#)]
15. Kolics, A.; Besing, A.S.; Wieckowski, A. Interaction of chromate ions with surface intermetallics on aluminum alloy 2024-T3 in NaCl solutions. *J. Electrochem. Soc.* **2001**, *148*, B322. [[CrossRef](#)]
16. Kermanidis, A.T.; Petroyiannis, P.V.; Pantelakis, S.G. Fatigue and damage tolerance behaviour of corroded 2024 T351 aircraft aluminum alloy. *Theor. Appl. Fract. Mech.* **2005**, *43*, 121–132. [[CrossRef](#)]
17. Petschke, D.; Lotter, F.; Staab, T.E.M. Revisiting the crystal structure of the equilibrium S (Al₂CuMg) phase in Al–Cu–Mg alloys using X-ray absorption spectroscopy (XAFS). *Materialia* **2019**, *6*, 100341. [[CrossRef](#)]
18. Ren, J.; Zuo, Y. Study of electrochemical behavior and morphology of pitting on anodized 2024 aluminum alloy. *Surf. Coat. Technol.* **2004**, *182*, 237–241. [[CrossRef](#)]